IN-PLASMA ANALYSIS OF PLASMA-SURFACE INTERACTIONS

P. Vinchon[1], S. Asadollahi[3], C. Coté[3], S. Marcet[2], S. Atallah[1], É. Dessureault[1],
M. Chicoine[1], A. Sarkissian[3], R. Leonelli[1], S. Roorda[1], F. Schiettekatte[1], L. Stafford[1*]

[1] Département de Physique, Université de Montréal, Montréal, Québec, CANADA
[2] Photon Etc., Montréal, Québec, CANADA

[3] Plasmionique inc., Varennes, Québec, CANADA

Abstract

During deposition, modification, and etching of thin films and nanomaterials in reactive plasmas, many active species can interact with the sample simultaneously. This includes reactive neutrals formed by fragmentation of the feed gas, positive ions and electrons generated by electron-impact ionization of the feed gas and fragments, excited states (in particular, long-lived metastable species), and photons produced by spontaneous de-excitation of excited atoms and molecules. Notably, some of these species can be transiently present during the different phases of plasma processing such as etching of thin layer deposition. To monitor plasma-surface interactions during materials processing, a new system combining beams of neutral atoms, positive ions, UV photons, and a magnetron plasma source has been developed. This system is equipped with a unique ensemble of *in-plasma* surface characterization tools including 1) a Rutherford Backscattering Spectrometer (RBS), 2) an Elastic Recoil Detector (ERD), and 3) a Raman spectroscopy system. RBS and ERD analyses are carried out using a differentially pumped 1.7 MV ion beam line Tandetron accelerator generating a beam at grazing incidence. The ERD system is equipped with an absorber and is specifically used to detect H initially bonded to the surface; higher resolution of surface H is also available through nuclear reaction analysis. In parallel, an optical port facing the substrate is used to perform Raman spectroscopy analysis of the samples during plasma processing. This system enables fast

[*] Electronic mail : luc.stafford@umontreal.ca

monitoring of a few Raman peaks over nine points scattered on a 1.6×1.6 mm^2 surface without interference from the inherent light emitted by the plasma. Coupled to the various plasma and beam sources, the unique set of *in-plasma* surface characterization tools detailed in this study can provide unique time-resolved information on the modification induced by plasma. By using the ion beam analysis capability, the atomic concentrations of various elements in the near-surface (e.g. stoichiometry and impurity content) can be monitored in real-time during plasma deposition or etching. On the other hand, the evolution of Raman peaks as a function of plasma processing time can contribute to a better understanding of the role of low-energy ions in defect generation in irradiation-sensitive materials such as monolayer graphene.

Keywords: Plasma processing of materials, Plasma-surface interactions, Raman spectroscopy, Ion Beam Analysis

1. Introduction

Upon contact with a plasma, the local equilibrium at the surface of a material is disrupted due to transient transfers of relatively large amounts of energy (up to several tens of eV) from neutral, ion, metastable, and photons. In addition to inducing surface defects, such energy transfer processes can initiate surface reactions that are beneficial for many applications[1,2]. Consequently, controlling plasma-surface interactions at the substrate surface and the reactor walls is of prime importance for many plasma processes, particularly during nanoscale device fabrication for which restrictions become stringent [3]. Low-pressure plasmas typically used for plasma deposition and etching of thin films and nanomaterials contain various energetic species such as ions, electrons, metastable species, photons, and reactive atomic and molecular neutrals. Even though some of these species are desirable for either deposition or etching, others can negatively impact the desired process. For example, ions accelerated by the plasma sheath acquire a significant amount of kinetic energy (up to 10-20 eV depending on experimental conditions) and thereafter induce bombardment on surfaces. Such very low-energy ions are also named hyperthermal. They can generate significant defects in materials and have a considerable impact on device performance [4,5]. Plasma-generated photons in the UV or VUV range can also significantly alter materials: while this is a useful function for medical sterilization applications [6], it can also provoke undesirable damage to the substrate [7–10]. As for metastable species, they can play an important role in the generation of defects on the surfaces of low-dimensional materials such as semiconductor quantum dots [11] and monolayer graphene films [5,12]. Furthermore, the complexity of plasma-surface interactions significantly increases with the introduction of molecules in the plasma. Upon fragmentation by electrons, resulting reactive species may lead to the deposition of a thin layer or to substrate etching, depending on the outcome of the chemical reactions occurring at the substrate surface [13,14]. Since all plasma-generated species interact simultaneously with plasma-exposed surfaces, synergetic effects can arise, resulting in process outputs that are often greater than the sum of the species' individual contributions [12,14].

In this work, we present the details of an innovative setup dedicated to the fundamental study of plasma-surface interactions involved in plasma deposition and etching of thin

films and nanomaterials. The proposed setup is equipped with several plasma sources that are designed to generate tightly controlled populations of neutral atoms and/or ions. This allows the deconvolution of the usually combined effects of plasma-generated species on material surfaces. To effectively estimate those individual contributions, the system is equipped with two material characterization methods: Raman spectroscopy and Ion Beam Analysis (IBA). The former provides insight into the vibrational environment of materials, while the latter enables the determination of atomic depth profiles and hydrogen concentrations near the surface are determined by Rutherford Backscattering Spectroscopy (RBS) and Elastic Recoil Detection (ERD). We demonstrate how these two methods can be deployed during plasma treatment with very little interference from the plasma. Such *in-plasma* characterization schemes allow for time-resolved measurements which are promising for the exploration of plasma-surface interactions' rich physic. By combining *in-plasma* material characterization methods with beams composed of plasma-generated species, a better understanding of the physical and chemical phenomena driving plasma-surface interactions at the atomic scale may be obtained.

2. Experimental details

2.1. Plasma sources

The setup consists of a hemispherical chamber equipped with up to four plasma sources (#1, #2, #3, and #4 in Fig.1a), all of which are oriented at a 45° angle relative to the target sample normal (Fig.1b). In this study, we make use of three 13.56 MHz Inductively Coupled Plasma (ICP) sources (#1, #2, and #3) and one magnetron sputtering source (#4). Source #1 produces a plasma that freely diffuses into the chamber, while source #2 is equipped with a polarized grid that generates a beam with a relatively broad Ion Energy Distribution Function (IEDF) when a positive voltage is applied. Source #3 has two grids at its exit, the first of which is in contact with the plasma and can be positively polarized, while the second is connected to ground potential. The resulting ion beam is less intense than the one produced by source #2, but its IEDF is narrower. Depending on the working pressure, sources #2 and #3 can generate ion or neutralized beams due to the ion-neutral

collisions occurring before the ions reach the substrate. Finally, source #4 is a magnetron sputtering source that enables thin film deposition.

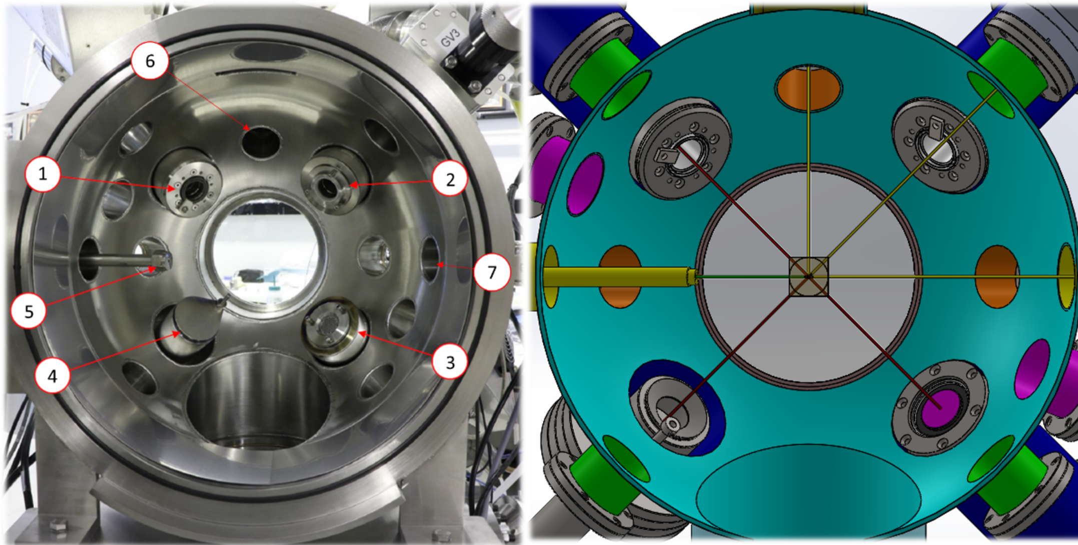

Figure 1: a) Picture of the setup in line with the sample position showing the exits of 1) source #1 (plasma), 2) source #2 (ion/neutral beam), and 3) source #3 (ion/neutral beam), as well as 4) magnetron plasma, 5) cannula introducing the high energy ion beam for IBA analysis, 6) entrance of the RBS detector (without the cone for reduced conductance; see text), and 7) entrance of the ERD detector (shown here without the absorber foil). b) Scheme of the chamber in the same view as a) but including a "backside view" of the sample (the square in the middle). This scheme shows that all instruments are pointed to the center where the substrate is located. The inner diameter of the chamber is 50 cm.

The sample holder is directly mounted on the door of the chamber. Once the latter is closed and the chamber is at low pressure, the sample is placed right in the middle of the hemisphere. The distance between each plasma source and the sample is typically 10–20 cm, and it can be tuned manually by moving each plasma source along its axis. The sample holder can be easily changed, depending on the requirements of the experiment. A heated sample holder (up to 800°C) is used herein; however, another substrate holder is designed to carry out precise hydrogen detection through the $p(^{15}N, \alpha\gamma)^{12}C$ Nuclear Resonant Reaction Analysis (NRRA) using an Ortec 905-4 scintillation detector with a 3x3" NaI(Tl) placed a few mm behind the sample. The heating sample holder is electrically isolated from the rest of the setup enabling the measurement of the ion current during IBA and the determination of the ion dose for each experiment. Even though IBA is considered not destructive, care must be taken to avoid using too high an ion dose which could generate

undesirable material defects. The effect can be monitored by acquiring spectra every minute.

The base pressure of the system is in the mid-10^{-7} Torr. Such base pressure is typical for plasma treatments or deposition where the working pressure, of several mTorr, is 10^4 times larger, so the ambient impurities represent a fraction of the gas impurities. Before the gas is introduced, the surface is exposed to impurities at rates reaching a few monolayers per minute. But it is worth noting that samples are introduced in the chamber from the ambient room, and the bombardment of these impurities occurs at thermal speeds, at energies and fluxes significantly lower than plasma bombardment, with much fewer reactive species. However, such impurities weakly bonded to the surface are not detected by IBA and Raman analyses. The former depth-resolves surface and subsurface features, surface contamination being commonly monitored, while the latter is mostly affected by the vibrational properties of the material. If any influence from surface impurities may be observed, namely when studying 2D materials, this system can significantly contribute to the understanding of such effects.

2.2. Ion beam analysis

The system is also equipped with Ion Beam Analysis (IBA) tools, such as a Rutherford Backscattering Spectrometer (RBS) and an Elastic Recoil Detector (ERD), that enable the precise detection of material composition [15,16] and light element concentrations at the surface [17]. The 1.7 MV Tandetron accelerator can generate ion beams of numerous elements in the periodic table, at up to 5.1 MeV for He and higher for elements allowing a higher charge state. To prevent a significant increase in beamline pressure due to the gas pressure in the plasma chamber (~10 mTorr), a differential pumping section is used to connect the beamline to the materials processing system. This pumping section maintains the beamline pressure at $<10^{-7}$ Torr. The generated ions transit through a long cannula (#5 in Figs. 1 and 2), which limits gas conductance, and they cross the plasma over 10 cm before hitting the substrate at an angle of 15°. Scattered ions are detected using a Passivated Implanted Planar Silicon (PIPS, #6) detector with a 14 keV resolution placed in a plane perpendicular to the beam/surface normal plane and oriented at a 45° angle with respect to the surface, enabling RBS. Meanwhile, recoiled hydrogen atoms are detected with a similar

detector but placed in the same plane as the beam and surface normal and oriented at a 15° angle with respect to the surface (#7), enabling ERD. A thin aluminum membrane placed in front of the ERD detector is used to absorb scattered primary ions, thereby ensuring that only hydrogen atoms reach the detector [18]. As the ion beam is oriented at a 15° angle with respect to the surface, the beam forms an oval spot on the sample 1.0 mm in height and 3.8 mm in width.

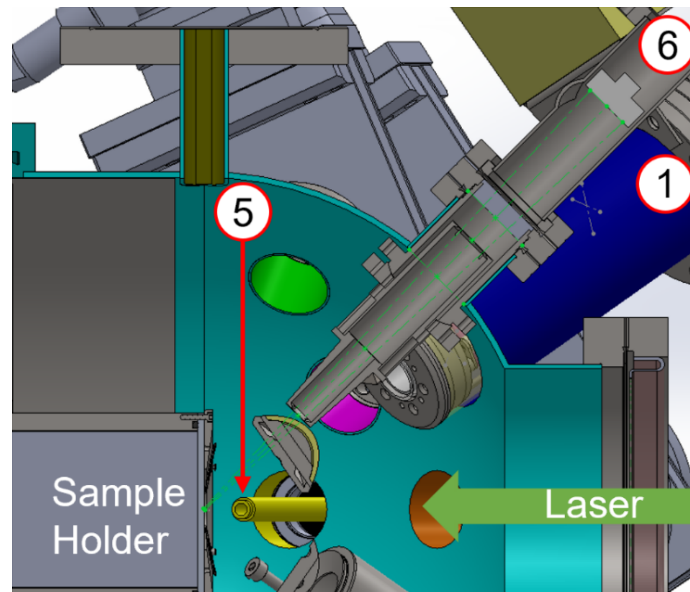

Figure 2: Side view scheme of the chamber showing 1) source #1, 5) the canula through which high energy ion beams enter the chamber and 6) the position of the RBS detector and cone used to reduce gas conductance. The laser for Raman spectroscopy is going into the chamber via a quartz window (right) and is focused on the sample holder. The distance between the sample center and the circular chamber walls is 25 cm.

RBS and ERD measurements are usually carried out at very low pressure (~10^{-7} Torr) to obtain high-resolution spectra. However, our chamber typically operates at a much higher pressure (10 mTorr), resulting in the generation of plasma discharges by the RBS and ERD PIPS detectors (biased at 50 V). To avoid such an issue, the detectors are separated from the chamber by a pumping section whose pressure is maintained by a turbomolecular pump. The aluminum membrane used to stop scattered primary ions from reaching the ERD detector also ensures that no gas from the chamber enters that section of the system. In the case of the RBS detector, it is not possible to use such a membrane, as it would significantly degrade the depth resolution. To circumvent this issue, a cone containing

baffles with small apertures is placed in front of the RBS (#6 in Fig. 2). This element effectively reduces the conductance and allows for RBS measurement without a membrane. However, it imposes a smaller solid angle, resulting in reduced statistics. As explained later in this article, the pressure in the pumped detector section is more than one order of magnitude lower than that inside the plasma chamber, sufficiently low to avoid discharges near the detectors.

2.3. Raman spectroscopy

The Raman setup is based on conventional confocal Raman microscopy but adapted for *in plasma* measurements. As shown in Fig. 3a, a 532 nm laser beam is first telescoped and diffracted by a Diffractive Optic Element (DOE) into nine main beams. These beams are reflected by a dichroic mirror and focused through a matrix of 50 µm nine-point pin holes distributed in a 1.6×1.6 mm^2 square that is slightly rotated by 18.3 degrees. Once it passes through the pinhole, each laser beam is focused on the sample using a series of lenses, the last of which is placed 24.6 cm away from the sample. The Raman light reemitted by the sample follows the exact same optical path as the incident light beam but is not reflected by the dichroic mirror. Instead, it passes through a series of lenses and a high-pass filter to produce a parallel beam. The latter is introduced into an Isoplane SCT 320 spectrometer whose slit is wide open. The nine parallel beams are diffracted by a grating before being focalized on a CCD camera. Here, the slight rotation of the square is of importance. Each beam produces a line after diffraction, and the chosen spatial beam distribution avoids any superposition of the diffracted line. As a result, all nine lines are detected by the camera, each corresponding to a sample spot probed by one of the nine laser beams. Currently, the system is equipped with an 1800 gr/mm grating that enables high spectral resolution measurements over a relatively narrow range (1.5 cm^{-1} over a 571 cm^{-1} range), as well as a 600 gr/mm grating used for low-resolution detection (5.9 cm^{-1}) over a wide wavenumber range (60 nm–1500 cm^{-1}). The difference in resolution between the two gratings can be observed in Fig. 3b, which shows the 546 nm emission lines issued from a low-pressure Hg lamp. A Gaussian function is used to determine the full width at half maximum

(FWHM) of the peak. Measurements taken with 600 and 1800 gr/mm gratings provide FWHM of 0.23 (8 cm^{-1}) and 0.072 nm (2.4 cm^{-1}) respectively.

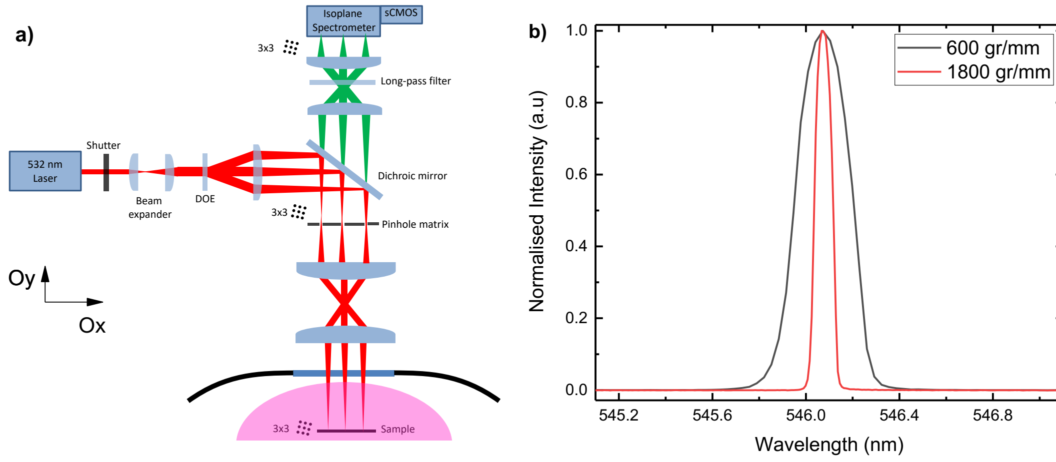

Figure 3: a) Scheme of the Raman setup geometry showing the excitation (red) and collection (green) beams. b) Normalized peak of a Mercury lamp obtained with a 600 gr/mm grating (black) and an 1800 gr/mm grating (red).

Finally, the diffracted light is imaged using a CMOS Hamamatsu OrcaFLash4.0 V3 camera. Although the maximum available laser intensity is 2.5 W, some loss inevitably occurs due to the DOE and the pin-hole matrix. Consequently, 60% of the initial laser power effectively reaches the sample. The laser focus on the sample is adjusted by changing the position of the last lens, whose relatively large diameter (8 cm for a focal length of 25 cm) allows for a small numerical aperture (i.e., detection of an 8 µm wide point on the substrate). This lens is placed on a long moving arm that controls its position on the (Oy) axis. The focus is considered satisfactory when the Raman intensity of one of the studied peaks (e.g., the 520 cm^{-1} peak of crystal Si) is maximized. The maximum integration time of the camera is 10 s; however, weak Raman signals can be observed by averaging several measurements.

The nine laser beams divided by the DOE can be used for simultaneous Raman detection at different locations on the sample. One must note that it can be difficult to align the sample with all nine beams, especially when 2D materials are involved. This difficulty is also present when attempting to probe the same region with both Raman spectroscopy and IBA. At most, only two to three Raman points could probe the region analyses by IBA.

Figure 4a shows the CCD image corresponding to the Raman measurement of a graphene monolayer grown on SiO_2 by chemical vapor deposition [19], using a 2.1 W laser power. Considering that 40% of the power is lost in the system and that the remaining power is divided into nine beams, a maximal power density of $P_{max} = 2.7\times10^9$ W/m^2 is estimated for each point. In this case, the use of the 600 gr/mm grating is pertinent, since its wide detection range allows for the simultaneous detection of all main graphene emission lines. In Fig. 4a, nine lines can be observed in the (Ox) direction, each corresponding to one of the nine diffracted beams. The intense spots distributed on these horizontal lines correspond to the emission bands that originate from Raman scattering (graphene), as well as from other sources. Fig. 4b depicts an image acquired with a closed stainless-steel

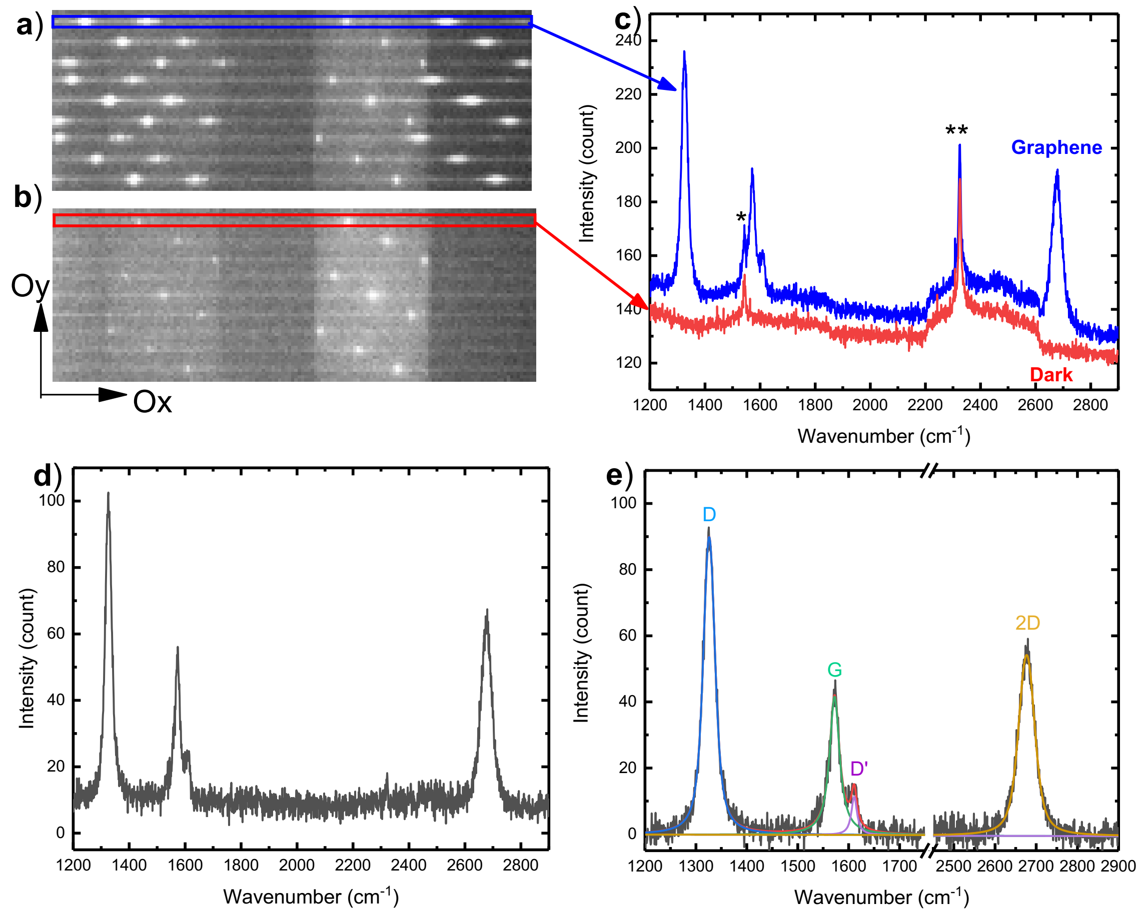

Figure 4: CCD images recorded a) when a Raman spectrum of a defected graphene monolayer is obtained and b) when the shutter is placed in front of the sample, named as dark. c) Spectra extracted from the region of interest delimited by the blue square (Fig.4a) and red square (Fig.4b). d) Spectra obtained by subtracting the two curves shown in Fig.4c. e) Voigt and Lorentzian function fits of the main Raman peaks (D, G, D', and 2D) in the subtracted spectrum.

shutter placed in front of the graphene sample. Even though no Raman scattering can be produced in this case, some peaks are still observed. These peaks correspond to artifacts originating from the optical system.

The peaks observed in Fig. 4a, but not in Fig. 4b, are attributed to graphene Raman scattering, as discussed below. Furthermore, Figs. 4a and 4b exhibit two wide bands along the (Oy) axis. These bands are ascribed to the parasitic light entering the spectrometer through the wide, open slit used to transfer all nine beams to the grating. Notably, the parasitic light reaches the spectrometer despite the stainless-steel sarcophagus covering the system. Figure 4c presents the spectra obtained by averaging the pixels in the sections delimited by blue and red rectangles in Fig. 4a, along the (Oy) direction. Graphene's Raman and artifact peaks (identified by * and **, respectively) can be easily distinguished. Moreover, a global shift in intensity is observed when Raman measurements are recorded. Since the artifact peak intensities are remarkably stable over time, the background spectrum – dark presented in Fig. 4c – can be subtracted from the Raman spectrum. In the case of time-resolved measurements, the setup alignment changes over time, resulting in similar backgrounds but with slight variations in absolute intensity. To circumvent this issue, the background spectrum must be corrected by a factor equivalent to the intensity ratio of the ** artifact peak in the Raman spectrum to that in the background spectrum. The resulting spectrum presented in Fig. 4d shows that even after removing the artifacts, a slight slope is observed in the background. This slope may be eliminated by fitting the curve to a 2nd-order polynomial function. Fig. 4e depicts the final corrected spectrum along with the fits of the four main graphene emission bands: D (1330 cm^{-1}), G (1575 cm^{-1}), D' (1610 cm^{-1}), and 2D (2670 cm^{-1}) [20]. By fitting these bands with the appropriate functions, their intensity, FWHM, and position values may be obtained. Herein, the D and 2D bands are fitted with a Voigt function, while the G and D' bands are correctly reproduced by a Lorentzian function.

As mentioned previously, the upper line delimited by the blue square in Fig. 4a is the result of the diffraction of one of the nine beam points. The spectral calibration of this point is straightforward and can be performed by using a well-known calibration lamp. The eight other points' wavelength calibrations are done relatively to the first point. Since the

geometric position of each beam across the 1.6×1.6 mm^2 square is well known, it is possible to determine the distance separating the nine beams arriving at the camera. Consequently, spectral calibration of the eight other points is done relatively to the first point before proceeding to data treatment.

3. *Plasma's influence on material characterization*

To assess the effect of the plasma on the ion beam and Raman measurements, two experiments were conducted. First, the sample was analyzed by RBS in the presence or absence of gas in the reactor chamber. Then, Raman spectra were recorded with the plasma turned on or off.

3.1. Rutherford backscattering spectroscopy with and without gas

The system employed in this study is designed to perform material characterization during plasma exposure. RBS combined with ions beam etching [21,22] as well as for the development of atmospheric RBS systems [23] have already been demonstrated. *In-plasma* IBA has also been reported, focusing on material modifications under extreme conditions as observed in nuclear fusion [24,25]. To assess the influence of the plasma on the recorded RBS spectra, a sample composed of a VO_2 layer (130 nm) deposited on a SiO_2 layer (260 nm) on Si substrate was analyzed in the presence or absence of the plasma. The latter should have a very limited influence on the sample composition, inducing only limited sputtering since ions energy is so low. It allows the observation of plasma influence on the RBS method only. At first, RBS analysis was conducted under a high vacuum in the chamber (6.6×10^{-7} Torr) and in the detector section (4.0×10^{-7} Torr). A 2 MeV Helium beam was introduced into the chamber via the differential pumping section, which was kept at 4.5×10^{-7} Torr. Once the first RBS measurement was completed, an argon ICP plasma was generated in the main chamber at 10 mTorr working pressure and 200 W power, thereby increasing the pressure in the detector section and differential pumping section to 9×10^{-4} and 1.4×10^{-5} Torr, respectively. Notably, the pressure inside the beamline did not change after plasma ignition (1×10^{-7} Torr), which confirms that the differential section acts as an effective buffer against the relatively high pressure in the plasma chamber. Upon generating the plasma, a second RBS measurement is acquired (one

should note that such plasma should not significantly affect the structure or composition of the sample). Fig. 5a presents the normalized RBS measurements of the same VO_2/SiO_2 sample recorded at low pressure (blue line) and in the presence of a plasma (red line). For clarity, a zoomed image of the vanadium peak is shown in Fig. 5b.

The presented spectra show that the composition of the sample is not altered upon exposure to plasma and that the sample is composed of vanadium, silicon, and oxygen (backscattering energies of 1661, 1299, and 1050 keV, respectively). Since the vanadium peak is well isolated, it can be used to observe the effects of the plasma. In Fig. 5a, the vanadium peaks recorded in the presence (blue spectrum) or absence of plasma (red spectrum) seem to be identical. However, the zoomed illustration in Fig. 5b reveals that plasma exposure slightly shifts the peak towards lower energy (by 5.5 keV). This shift is mainly attributed to the electronic energy losses of He incident and scattered ions upon traveling through a 40 cm of Ar. Based on SRIM calculation, 2 MeV He ions are expected to lose around 0.9 keV which is significantly below the shift observed here. Other losses may originate from collisions in the differential pumping section as well. Considering that no other change is observed and that the peak shape and resolution are preserved during exposure to the plasma, it may be concluded that plasmas generated at the working pressure of 10 mTorr have very little influence on RBS measurement. Consequently, subsequent *in-plasma* RBS measurements may be carried out without concern.

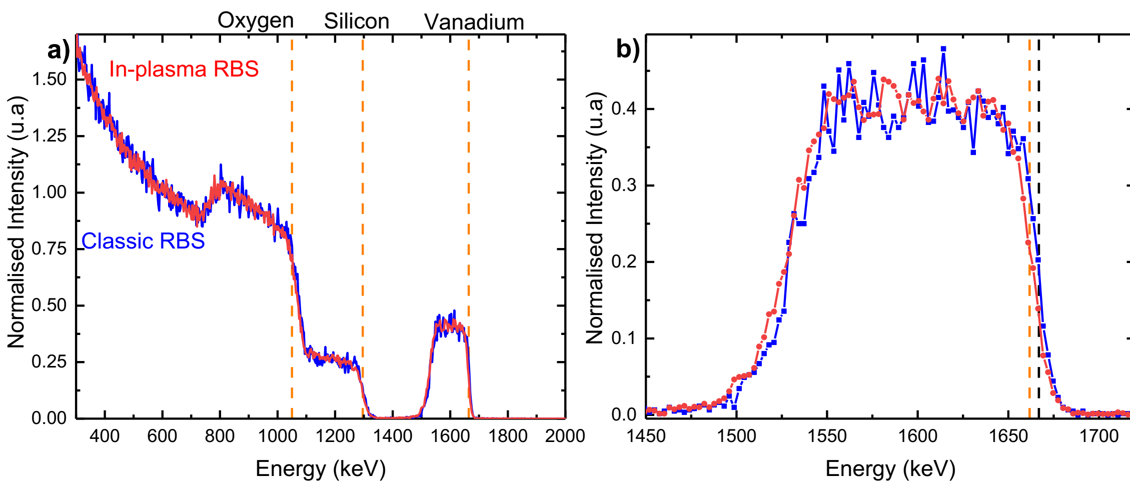

Figure 5: a) Full RBS spectrum and b) zoomed vanadium peak obtained under high vacuum (blue curve) and with an argon plasma at 10 mTorr (red curve).

Considering that the scattering laser light reflected on the substrate at a certain angle may blind the RBS detector, it might not be possible to record Raman and RBS spectra simultaneously, over the exact same location. This issue can be mitigated by displacing the laser spots a few mm away from the ion beam spot, or by slightly tilting the sample. Still, to avoid any interference, it is best to alternate the Raman and RBS measurements. Since the ERD detector is placed behind an aluminum membrane, ERD measurements are not affected by the light from the laser. Furthermore, these measurements are not influenced by plasma, just like the RBS measurements. This confirms that *in-plasma* RBS and ERD measurements can be performed simultaneously. If the incoming ion beam is sufficiently intense, it is possible to achieve time-resolved measurements, as discussed below.

3.2. *In-plasma* Raman spectroscopy

The excited species generated in a plasma emit light of a specific wavelength as they deexcite to a lower energy state. Such light, if sufficiently intense, can hinder Raman measurements. Consequently, while in-situ Raman spectrometry is relatively common [26,27], the implementation of *in-plasma* Raman system to obtain time-resolved measurements is still lagging [28,29]. Source #1 generates a plasma that can freely diffuse into the chamber and reach the sample. Hence, some light will be emitted near the sample and may be detected by the Raman spectrometer. The intensity detected depends on the experimental conditions such as gas nature, pressure, and power. In contrast, the electrons generated by plasma source #2 are attracted to the positive grid, leading to a decreased density of excited species in the vicinity of the substrate. As for the plasma generated by source #3, it is confined by the two grids positioned at its exit. Consequently, only the plasma generated by source #1 can produce light that may alter the Raman measurements. This is especially true if the studied material has poor Raman scattering efficiency and does not tolerate high laser power. In this case, a long integration time is necessary to obtain a satisfactory signal. Herein, the effect of the light emitted by plasma source #1 was eliminated by subtracting the optical emission spectrum measured without the laser from the one measured with the laser focused on a SiC sample. As presented in Fig. 6a, both spectra were recorded in the presence of an Ar plasma generated by source #1(300W – 5 mTorr and an Ar flow of 20 sccm), and a shutter was used to control

the entry of laser light into the Raman system (Fig. 3a). The resulting spectrum from the subtraction of both spectra from Fig. 6a is presented in Fig. 6b. An integration time of 4 s was found to be adequate for Raman measurement in the presence or absence of laser.

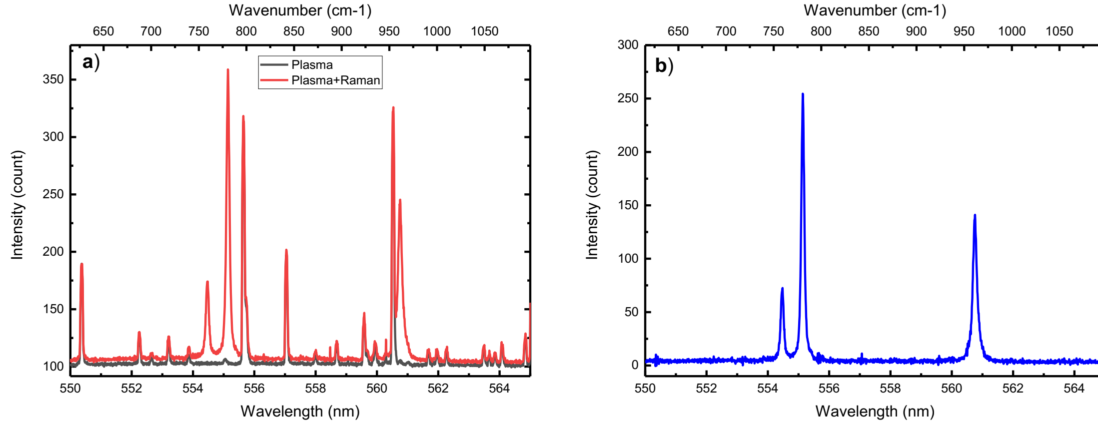

Figure 6: a) Optical measurements acquired in the presence of an Argon plasma with the laser focalized on SiC substrate (red) and without laser (black). b) Spectrum obtained by subtracting the two curves presented in a).

As shown in Fig. 6a, the Raman spectrum recorded with an open shutter (“Plasma+Raman” spectrum displayed in red) exhibits numerous peaks that cannot be easily attributed to the substrate or the plasma. However, when the shutter is closed and the laser light is cut off (“Plasma” spectrum displayed in black), the peaks at 555.1, 555.6, and 570.8 nm (783, 799, and 964 cm^{-1}, respectively) disappear. This indicates that these peaks correspond to Raman scattering of the substrate. Indeed, they are characteristic emission peaks of 6H-polytype SiC [30,31]. The remaining emission lines in the “Plasma+Raman” spectrum are not affected by the absence of the laser, which suggests that they are attributed to the excited species generated by the plasma. Furthermore, a global negative shift in the background can be observed when the laser is cut off. The subtracted spectrum shown in Fig. 6b features three peaks characteristic of SiC, as mentioned above. The background of this spectrum is slightly above zero; however, a higher background is observed where important plasma emission lines are present, because of subtraction in increasing the statistical noise. Still, Fig. 6b presents a typical SiC Raman spectrum that can be easily fitted to extract the peak intensity, FWHM, and position values.

Although the subtraction method employed herein yields satisfactory results, it has some drawbacks. For instance, it decreases the temporal resolution of time-resolved measurements, since two optical measurements are needed (with and without laser). Furthermore, as mentioned previously, this method is efficient only if the plasma reaches a steady state, resulting in minimal timescale variations between two measurements. Finally, if the Raman scattering is very weak compared to the plasma emission, the subtraction method will be less reliable. Nevertheless, since we tested this method with the most luminous plasma available, *in-plasma* Raman measurements performed using the method developed herein may be considered plausible. In fact, the subtraction method is not even necessary when using source #3, and it is only needed under certain conditions when plasma source #2 is applied. Finally, this method becomes unreliable if molecules are introduced in the plasma, generating numerous vibrational and rotational bands. In this case, it would be best to go toward other methods found in the literature which focus for example on synchronized pulsed Raman measurements [28,29].

In-plasma Raman spectroscopy is typically used to analyze material evolution during plasma modification. However, one must be aware that the laser itself might influence the process initiated by the plasma. This could lead to the misinterpretation of Raman spectra. To ensure that the laser has no influence, the measurements must be repeated with different laser frequencies or power densities.

4. Time-resolved *in-plasma* surface monitoring

4.1. Monitoring of thin film growth by IBA

As mentioned in section 3.1, *in-plasma* RBS and ERD analyses can be achieved with very little loss in resolution, which allows for the monitoring of thin film growth. As indicated in section 1.1, the system is equipped with a magnetron plasma source that is commonly used to deposit thin films of amorphous silicon (*a*-Si)[32] or silicon dioxide (*a*-SiO_2) [33,34]. RBS is an ideal characterization tool that can be used to determine the nature of the element deposited and the stoichiometry of the plasma-deposited layer. Meanwhile, ERD provides insight into the concentration of hydrogen, an element whose depth profile cannot be easily determined using other analytical techniques. Herein, SiO_2 was deposited

on a Glass Like Carbon (GLC) substrate by exposing the silicon target to an O_2/Ar (2/20 sccm) plasma and then to a pure Ar plasma. The working pressure was set at 10 mTorr and the incident power at 80 W. After 33 min of plasma deposition, the oxygen flow was cut off, thereby causing an increase of the bias from 314 to 400 V. The sample was exposed to a 2 MeV He ion beam during the entire experiment to obtain the RBS and ERD spectra, which were saved every minute. Figs. 7a and 7b present the RBS and ERD spectra (averaged over 5 min) recorded at different times during the plasma deposition process, respectively.

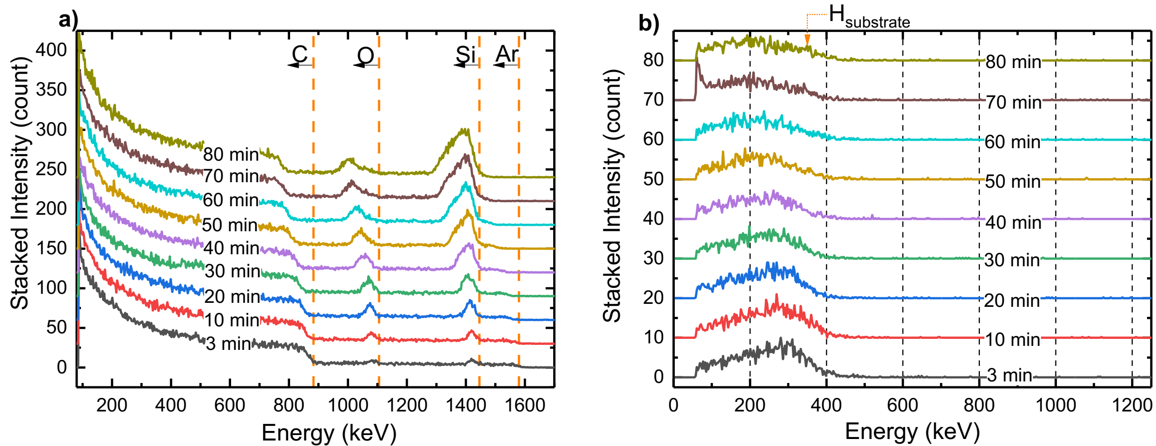

Figure 7: 5-min-averaged in-plasma a) RBS and b) ERD spectra recorded at different times during Magnetron sputtering deposition of Si in an Ar:O2 atmosphere, with decreasing amount of O2 (see text).

As shown in Fig. 7a, the RBS spectrum acquired after 3 min of deposition exhibits four signals. The signal at 880 keV corresponds to the most abundant element on the GLC surface, C. The background signal appearing at energies up to 1575 keV is attributed to the Ar atoms entrapped in the porous GLC substrate during its synthesis by plasma deposition (specified by the manufacturer). The two remaining peaks detected at 1450 and 1105 keV are ascribed to Si and O elements, respectively. At 30 min deposition time, the Si and O peaks become wider and more intense, indicating that the SiO_x layer has grown. The energy shifting of the C and Ar signal edges by 33 and 24 keV, respectively, further confirms the growth of the SiO_x layer on the substrate. As the oxygen supply (2 sccm) is cut off, the chamber is progressively filled with a pure argon plasma as the oxygen is pumped out. However, the intensity of the O peak keeps on increasing until it reaches a maximum after 50 min of deposition. Beyond this time, the peak remains stable. Moreover, at long deposition times, the O peak maximum shifts to lower energy, and an asymmetry appears.

This indicates that a new layer with a different stoichiometry is being deposited on top of the initial layer. The Si peak also becomes asymmetric at long times; however, unlike the O peak, its intensity keeps on increasing until the end of the experiment. Notably, the asymmetry of the Si peak mirrors that of the oxygen peak, as the peak maximum remains centered at the energy corresponding to the surface. As expected, the fraction of Si in the deposited film increases after shutting off the O_2 supply, leading to a peak that is more intense near the surface (higher energy edge) than at the substate interface (lower energy edge). The inverse is observed for the O peak. By the end of the experiment, the C and Ar signals have shifted by 88 and 133 keV, respectively, due to the presence of the plasma-deposited film.

The ERD spectrum acquired after 3 min of deposition (Fig. 7b) exhibits a broad peak below 426 keV, which indicates that the GLC substrate initially contains a significant amount of hydrogen. At longer deposition time, the upper limit of the peak slightly shifts towards lower energy, and it reaches 420 keV by the end of the experiment. This means that H is incorporated into the film during the deposition process. Indeed, a SIMNRA analysis [35] of the last ERD spectrum shows the hydrogen signal from the substrate is around 350 keV as indicated in Fig. 7b. Considering that the intensity of the peak decreases in the region corresponding to the deposited film (near 400 keV), less H is incorporated during deposition than during the synthesis of GLC. Although no H was intentionally introduced into the chamber, this element is known to be a pervasive impurity that cannot be easily eliminated by pumping.

A SIMNRA analysis of the 80 min RBS spectrum shows that a total of 3.3×10^{15} ions.cm^{-2} has probed the sample during the whole experiment. While this value is not too very large, it may still alter the deposited sample. Consequently, in similar future experiments, RBS measurements should be done on a neighboring spot at the end of plasma deposition to check if IBA does alter the studied process.

The stoichiometry of elements in the plasma-deposited thin film was determined based on the ratios of the corresponding RBS peaks to the peak summed over a certain range. To assess the composition of the surface layer, the peaks were summed over 55 keV (20 channels), an energy that is just below the surface energy. Meanwhile, the composition of

the whole layer was analyzed by summing over 137.5 keV (50 channels). To convert the counts into Si:O ratio, the Z^2 dependence of the Rutherford cross-section must be considered. Specifically, since peak intensity rises strongly with the element's atomic number, it must be divided by Z^2 to properly evaluate the elements' concentration[16,36]. Fig. 8a presents the evolution of the Si/((Si+O) and O/(Si+O) ratios (in percentage) corresponding to the surface region as a function of plasma deposition time. The evolution of the Z^2-normalized total signal intensities of Si and O is presented in Fig. 8b.

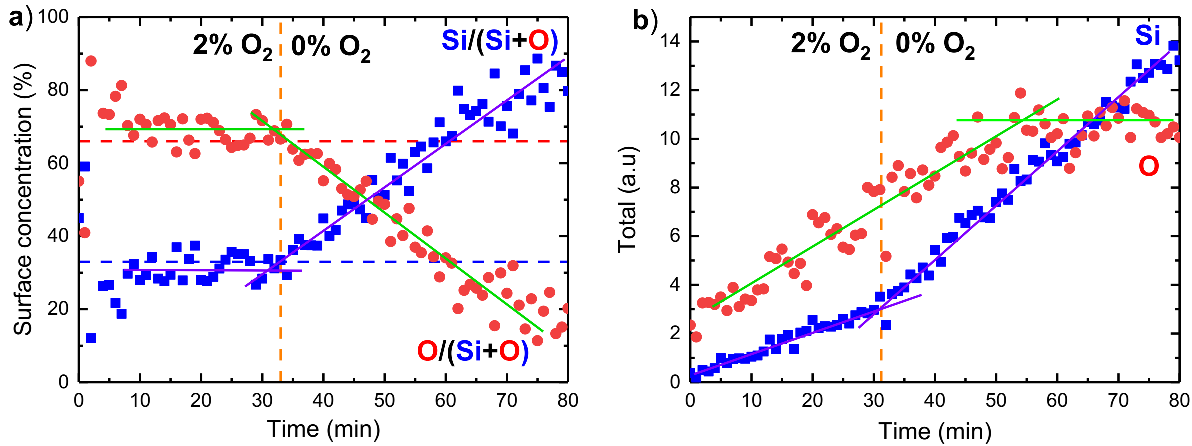

Figure 8: a) Temporal evolution of Si/(Si+O) (blue) and O/(Si+O) (red) in the surface region (summed over 55 keV). b) Temporal evolution of the Si (blue) and O (red) total peak area.

As shown in Fig. 8a, the relative concentrations of O and Si to the sum of the two fluctuate significantly during the first few minutes of deposition due to the proximity between the RBS peaks of these elements and the Ar background level. After 10 min, the peaks become stable, and after 20 min, the concentration of Si reaches ~33%, which indicates that SiO_2 is being deposited. When the oxygen supply is cut off at 33 min, the concentration of O declines, whereas that of Si increases. Since the deposition rate is rather low, the linear variation suggests that the surface layer is progressively shifting from SiO_2 to pure Si. This shift is relatively smooth, which suggests that oxygen remains in the plasma chamber for quite some time.

The results illustrated in Fig. 8b shows that the Z^2-normalized total signals of Si and O increase linearly with time. Note that the absolute signal values are not reliable since the background was not subtracted before summing the peaks. After cutting off the oxygen

supply at 33 min, the Si deposition rate immediately increases, but the O deposition rate remains the same until 53 min. Beyond this time, the O signal becomes saturated. Considering that the oxygen residence time at the working pressure of the plasma deposition experiment is estimated to be 6 ms, 20 min are needed to remove most of the oxygen from the chamber, which agrees well with the time-resolved RBS measurements. Since the total O peak remain constant for 20 min at the end of the experiment, it is expected that O surface concentration would eventually reach 0%. Even though Figure 8a shows a final O concentration of ~10-20% due to the weak Si deposition rate, it should eventually reach close to 0% had the experiment lasted longer. Overall, the RBS and ERD data show that real-time *in-plasma* measurements provide useful information regarding the evolution of thin layer deposition.

4.2. Graphene modification monitoring by Raman spectroscopy

The setup proposed herein can also be used to study ion- of plasma-induced defect generation in low-dimensional materials such as graphene. For instance, Raman spectroscopy is widely used to characterize graphene monolayers. As shown in Fig. 4, the main Raman bands of graphene are D, G, D', and 2D. Using a 532 nm laser (E_{laser} = 2.33 eV), these bands are detected at 1350, 1580, 1610, and 2690 cm^{-1}, respectively. The intensity line ratio of D to G (I_D/I_G) is commonly used to determine defect density [37,38]. By plotting the ratio of the D peak area to the G peak area (A_D/A_G; values corrected by the laser wavelength) as a function of the FWHM of the G peak (Γ_G), Cancado *et al.* [39] determined both, the defect nature and density. The same method was used in other studies to understand the defect generation kinetics by argon and nitrogen plasmas [5,12,40,41]. In these studies, monolayer graphene was exposed to numerous excited species such as low energy ions (2–15 eV), metastable species, VUV photons, and nitrogen atoms.

In our proposed setup, source #3 can be used to produce a beam of Ar ions whose energy is similar to that of the ions obtained following their acceleration in the sheath of low-pressure plasmas [5]. Metastable species and VUV photons can be neglected in this case, and only the effect of low-energy ions on the graphene state is observed (no synergetic effect with other plasma-generated species) using the *in-plasma* Raman spectroscopy system. Herein, the measurements were performed every 10 s with an integration time and

laser power of 4 s and 2.1 W, respectively. The statistics of the spectra obtained under these conditions are good enough to use the procedure presented in section 2.3. The subtraction method discussed in section 3.2 is not needed, since source #3 does not produce significant amounts of light close to the substrate. Consequently, the evolution of graphene can be followed during ion beam exposure. The ion beam was produced by a plasma generated at the working pressure of 5 mTorr and the excitation power of 50 W. To reproduce the ion bombardment process typical of the plasma condition, the first grid bias was set at 13 eV. Figs. 9a and 9b present the evolution profiles of I_D/I_G and Γ_G as a function of time, respectively, for eight Raman points recorded simultaneously (the ninth point is dismissed as it is probing an area outside the graphene sample). The Cancado-like plots described previously are shown in Fig. 9c.

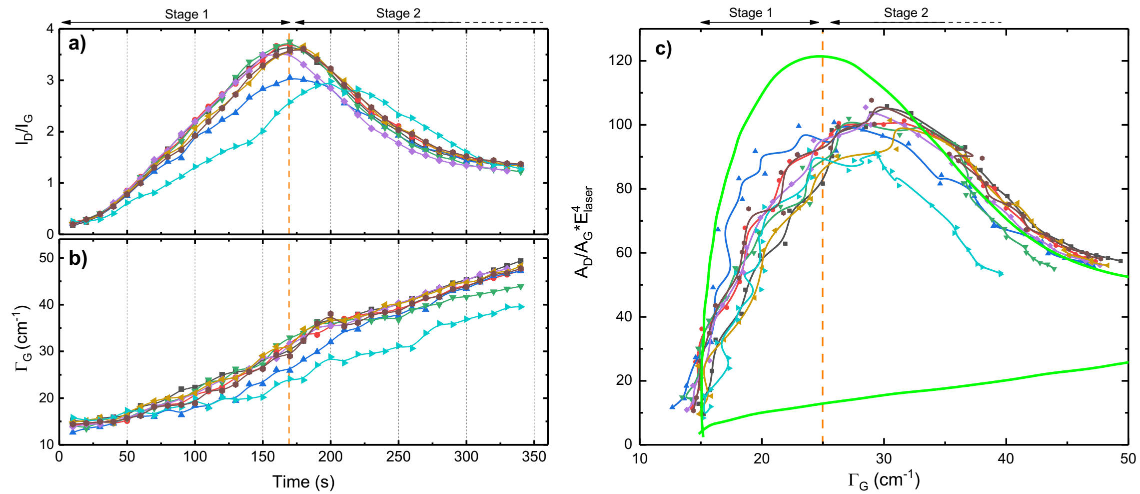

Figure 9: Temporal evolution of a) I_D/I_G and b) Γ_G for eight Raman points recorded simultaneously. c) Variation of A_D/A_G (corrected by the laser energy) as a function of Γ_G. Green curves: see text.

As shown in Fig. 9a, I_D/I_G increases linearly with time for all points. The profiles of six Raman points are almost superposed, with I_D/I_G ratios increasing from 0.1 to a maximum of 3.5 within 175 s of ion beam treatment. The two remaining Raman spots present slightly different behaviors, as one (in blue) reaches a maximum I_D/I_G value of 3 within 175 s, while the other (in cyan) reaches 2.9 within 200 s. Beyond the maximum, all ratios decrease and then stabilize at around 1.5. The overall behavior of I_D/I_G is typical of defect generation and is commonly observed in defective monolayer graphene. For instance, the increasing

ratio corresponds to "stage 1" graphene whose defect concentration is low, while the decreasing ratio is indicative of "stage 2" graphene whose defect concentration is very high [20].

Initially, the value of Γ_G is 13 cm^{-1}, irrespective of the analyzed spot on the substrate surface (Fig. 9b). For all investigated Raman spots, this value increases linearly to 35 cm^{-1} at 175 s, except in the case of the blue and cyan datasets. As shown in Fig. 9b, these profiles exhibit a lower rate of increase in Γ_G compared to the other profiles. Indeed, the blue and cyan profiles present Γ_G values of 32 and 29 cm^{-1}, respectively, at 200 s. Beyond this time, Γ_G rises even though at a lower rate for all cases. Of the six spots initially superimposed, five reach a value of around 45 cm^{-1} by the end of the experiment. The green (sixth spot), blue, and cyan datasets reach 40, 44, and 37 cm^{-1}, respectively. Notably, the inflection in the Γ_G evolution does not strictly coincide with the maximum of I_D/I_G. The evolution of Γ_G can be ascribed to defect concentration. However, Γ_G is also dependent on doping level [42], which makes its interpretations less straightforward than I_D/I_G.

The Cancado-like plots presented in Fig. 9c demonstrate that in the Γ_G range of 13–30 cm^{-1}, A_D/A_G increases from 15 to around 100 for all analyzed spots. Between 30 and 36 cm^{-1}, the area ratio decreases to 80, then it decreases further to 70 as Γ_G reaches 45 cm^{-1}. Since Γ_G increases monotonically with time, the plots in Fig. 9c also reflect the variation of the area ratio as a function of time. Similar evolution profiles are detected for all spots, even though the blue and cyan dataset profiles are slightly different. The former profile exhibits a maximum of ~100 at around 25 cm^{-1}, while the latter attains a maximum of 90 at around 30 cm^{-1}. To better understand the Cancado-like plots in Fig. 9c, they must be compared to the theoretical plot (fluorescent green), which can be obtained using the method described in Cançado *et al*. [39] depending on the nature of the generated defects. Typically, vacancies are considered 0D defects (top green curve), while cracks and grain boundaries are considered 1D defects (bottom green curve). As shown in Fig. 9c, the maxima of all experimental curves obtained herein (Γ_G = 30 cm^{-1}) are lower than that of the 0D theoretical curve (Γ_G = 25 cm^{-1}). This suggests that defect generation during the experiment is not purely 0D. Indeed, the Raman system probes a circular spot that is 8 μm wide and may

contain a mix of 0D and 1D defects. Similar results were reported for monolayer graphene exposed to a low-pressure argon plasma [5].

Since the sample is monolayer graphene grown by chemical vapor deposition, it inevitably comprises grain boundaries that can influence Raman measurements [21]. In principle, the 13 V acceleration applied herein cannot generate vacancy-type defects, as it is well below the estimated threshold barrier of 18–20 eV [43]. However, at such energy, the ion neutralization probability is relatively high and can provide significant local energy (up to 15.96 eV for Ar ions) to the surface. The mechanism behind such a phenomenon remains unclear, but this setup will enable more thorough studies that can shed light on defect formation and annealing kinetics following ion beam and plasma exposure. Considering that the nine studied points are distributed over a 1.6×1.6 mm^2 square, each point probes an essentially different area. Therefore, the obtained results may be used to assess the uniformity of the treatment. Herein, we show that five to six points probe graphene areas that may be considered identical (similar profiles in Figs. 9a, 9b, and 9c), while two points probe essentially different areas such as graphene edges. Still, it is not possible to distinguish between the areas based on their initial state, since the Raman parameters are relatively similar to those of the other points.

5. Conclusion

Although plasmas are universally used for material processing, the modification of materials by plasmas is often not fully understood. This is mainly due to the extremely complex interactions between the plasma-generated species and the sample. Considering the importance of miniature devices and low-dimensionality materials in technological applications, a fundamental understanding of plasma-surface interactions is crucial to control defect generation and kinetics. The hybrid setup presented in this paper is equipped with four plasma sources that generate ion and neutral beams, inductively coupled plasmas, and magnetron plasmas. *In-plasma* IBA and Raman spectroscopy systems are also incorporated into the setup, and they may be used to provide a detailed characterization of materials in the absence of ambient air exposure. *In-plasma* RBS and ERD measurements can also be performed, as the design of the setup achieves reduced pressure close to the

detectors. Herein, real-time *in-plasma* analysis of *a*-SiO_x deposition by magnetron sputtering is performed using IBA. Such analysis can be used to assess the fine changes in material composition during deposition. Although the plasma does not affect the RBS and ERD measurements, the laser from the Raman setup can bling the RBS detector. Therefore, experiments must be planned carefully to avoid any interference. Furthermore, *in-plasma* Raman spectra are obtained using a simple method that eliminates the emission lines of plasma-excited species, even when their intensities are comparable to those of the Raman peaks. To demonstrate the capabilities of the designed reactor, an experiment of defect generation in monolayer CVD-graphene by very low-energy argon ions is carried out using *in-plasma* Raman spectroscopy. The results of this experiment provide insight into defect generation in real-time, and they are in good agreement with the numerous studies published in the literature on graphene defects. The results also provide spatial information regarding the sample, which can be extremely useful for non-uniform samples, including low-dimensional materials with grain boundaries [40,41]. In general, the setup proposed herein constitutes an extremely powerful tool that can be used to study plasma-surface interactions and assess the fundamentals of material processing by plasma, thereby laying the foundation for the development of new nanomaterials.

Acknowledgment

This work was financially supported by the Canada Foundation for Innovation, the National Science and Engineering Research Council (NSERC), PRIMA-Québec, the Canada Research Chair, the Université de Montréal, and the Fonds de Recherche du Québec – Nature et Technologies (FRQNT).

Data Availability

The data that support the findings of this study are available from the corresponding author upon reasonable request.

Reference

[1] S. Tachi, Chemical sputtering of silicon by F+, Cl+, and Br+ ions: Reactive spot model for reactive ion etching, Journal of Vacuum Science & Technology B: Microelectronics and Nanometer Structures. 4 (1986) 459. https://doi.org/10.1116/1.583404.

[2] K. Ishikawa, T. Ishijima, T. Shirafuji, S. Armini, E. Despiau-Pujo, R.A. Gottscho, K.J. Kanarik, G.J. Leusink, N. Marchack, T. Murayama, Y. Morikawa, G.S. Oehrlein, S. Park, H. Hayashi, K. Kinoshita, Rethinking surface reactions in nanoscale dry processes toward atomic precision and beyond: A physics and chemistry perspective, Jpn J Appl Phys. 58 (2019). https://doi.org/10.7567/1347-4065/ab163e.

[3] V.M. Donnelly, J. Guha, L. Stafford, Critical review: Plasma-surface reactions and the spinning wall method, Journal of Vacuum Science & Technology A: Vacuum, Surfaces, and Films. 29 (2011) 010801. https://doi.org/10.1116/1.3517478.

[4] H. Li, T. Ito, K. Karahashi, M. Kagaya, T. Moriya, M. Matsukuma, S. Hamaguchi, Experimental and numerical analysis of the effects of ion bombardment in silicon oxide (SiO2) plasma enhanced atomic layer deposition (PEALD) processes, Jpn J Appl Phys. 59 (2020). https://doi.org/10.35848/1347-4065/ab8681.

[5] P. Vinchon, X. Glad, G. Robert-Bigras, R. Martel, A. Sarkissian, L. Stafford, A combination of plasma diagnostics and Raman spectroscopy to examine plasma-graphene interactions in low-pressure argon radiofrequency plasmas, J Appl Phys. 126 (2019) 233302. https://doi.org/10.1063/1.5125143.

[6] G.Y. Park, S.J. Park, M.Y. Choi, I.G. Koo, J.H. Byun, J.W. Hong, J.Y. Sim, G.J. Collins, J.K. Lee, Atmospheric-pressure plasma sources for biomedical applications, Plasma Sources Sci Technol. 21 (2012). https://doi.org/10.1088/0963-0252/21/4/043001.

[7] M.J. Titus, D. Nest, D.B. Graves, Absolute vacuum ultraviolet flux in inductively coupled plasmas and chemical modifications of 193 nm photoresist, Appl Phys Lett. 94 (2009) 92–95. https://doi.org/10.1063/1.3125260.

[8] J.R. Woodworth, M.G. Blain, R.L. Jarecki, T.W. Hamilton, B.P. Aragon, Absolute intensities of the vacuum ultraviolet spectra in a metal-etch plasma processing discharge, Journal of Vacuum Science & Technology A: Vacuum, Surfaces, and Films. 17 (1999) 3209. https://doi.org/10.1116/1.582044.

[9] S. Uchida, S. Takashima, M. Hori, M. Fukasawa, K. Ohshima, K. Nagahata, T. Tatsumi, Plasma damage mechanisms for low- k porous SiOCH films due to radiation, radicals, and ions in the plasma etching process, J Appl Phys. 103 (2008). https://doi.org/10.1063/1.2891787.

[10] J. Lee, D.B. Graves, Synergistic damage effects of vacuum ultraviolet photons and O2 in SiCOH ultra-low-k dielectric films, J Phys D Appl Phys. 43 (2010) 1–6. https://doi.org/10.1088/0022-3727/43/42/425201.

[11] J.A. Ferreira, H.P.T. Nguyen, Z. Mi, R. Leonelli, L. Stafford, Improvement of the emission properties from InGaN/GaN dot-in-a-wire nanostructures after treatment in the flowing afterglow of a microwave N2plasma, Nanotechnology. 25 (2014). https://doi.org/10.1088/0957-4484/25/43/435606.

[12] P. Vinchon, X. Glad, G.R. Bigras, A. Sarkissian, R. Martel, L. Stafford, Plasma–graphene interactions: combined effects of positive ions, vacuum-ultraviolet photons, and metastable species, J Phys D Appl Phys. 54 (2021) 295202. https://doi.org/10.1088/1361-6463/abfe3b.

[13] F. Fracassi, R. D'Agostino, Plasma deposition of silicon nitride-like thin films from organosilicon precursors, Plasmas Polym. 1 (1996) 3–16. https://doi.org/10.1007/BF02532811.

[14] J.W. Coburn, H.F. Winters, Ion- and electron-assisted gas-surface chemistry—An important effect in plasma etching, J Appl Phys. 50 (1979) 3189. https://doi.org/10.1063/1.326355.

[15] K. Kimura, K. Ohshima, M.H. Mannami, Monolayer analysis in Rutherford backscattering spectroscopy, Appl Phys Lett. 64 (1994) 2232–2234. https://doi.org/10.1063/1.111653.

[16] M. Nastasi, J.W. Mayer, Y. Wang, Rutherford backscattering spectrometry, CRC Press, 2014. https://doi.org/10.1201/b17310.

[17] W.M. Arnold Bik, F.H.P.M. Habraken, Elastic recoil detection, Reports on Progress in Physics. 56 (1993) 859–902. https://doi.org/10.1088/0034-4885/56/7/002.

[18] J. L'Ecuyer, C. Brassard, C. Cardinal, J. Chabbal, L. Deschênes, J.P. Labrie, B. Terreault, J.G. Martel, R. St.-Jacques, An accurate and sensitive method for the determination of the depth distribution of light elements in heavy materials, J Appl Phys. 47 (1976) 381–382. https://doi.org/10.1063/1.322288.

[19] X. Li, W. Cai, J. An, S. Kim, J. Nah, D. Yang, R. Piner, A. Velamakanni, I. Jung, E. Tutuc, S.K. Banerjee, L. Colombo, R.S. Ruoff, Large-Area Synthesis of High-Quality and Uniform Graphene Films on Copper Foils, Science (1979). 324 (2009) 1312–1314. https://doi.org/10.1126/science.1171245.

[20] A.C. Ferrari, D.M. Basko, Raman spectroscopy as a versatile tool for studying the properties of graphene, Nat Nanotechnol. 8 (2013) 235–246. https://doi.org/10.1038/nnano.2013.46.

[21] Z. Siketić, I. Bogdanović Radović, I. Sudić, M. Jakšić, Surface analysis and depth profiling using time-of-flight elastic recoil detection analysis with argon sputtering, Sci Rep. 8 (2018). https://doi.org/10.1038/s41598-018-28726-x.

[22] K.R. PADMANABHAN, In Situ Ion Beam Analysis of chemical and plasma etching of Si, Modern Physics Letters B. 15 (2001) 1419–1427. https://doi.org/10.1142/S0217984901003342.

[23] L. Pichon, L. Beck, P. Walter, B. Moignard, T. Guillou, A new mapping acquisition and processing system for simultaneous PIXE-RBS analysis with external beam, Nucl Instrum Methods Phys Res B. 268 (2010) 2028–2033. https://doi.org/10.1016/j.nimb.2010.02.124.

[24] F. Bedoya, K.B. Woller, D.G. Whyte, Study of the properties of thin Li films and their relationship with He plasmas using ion beam analysis in the DIONISOS experiment, Review of Scientific Instruments. 89 (2018). https://doi.org/10.1063/1.5034240.

[25] G.M. Wright, H.A. Barnard, L.A. Kesler, E.E. Peterson, P.W. Stahle, R.M. Sullivan, D.G. Whyte, K.B. Woller, An experiment on the dynamics of ion implantation and sputtering of surfaces, Review of Scientific Instruments. 85 (2014) 023503. https://doi.org/10.1063/1.4861917.

[26] G. Guimbretière, L. Desgranges, A. Canizarès, R. Caraballo, F. Duval, N. Raimboux, R. Omnée, M.R. Ammar, C. Jégou, P. Simon, In situ Raman monitoring of He2+ irradiation induced damage in a UO2 ceramic, Appl Phys Lett. 103 (2013). https://doi.org/10.1063/1.4816285.

[27] P. Brault Jacky Mathias, C. Lure, P. Ranson, O. Texier, In situ Raman spectroscopy of silicon surfaces during SF6 plasma etching Ll, 1994.

[28] C. Berrospe-Rodriguez, J. Schwan, G. Nava, F. Kargar, A.A. Balandin, L. Mangolini, Interaction between a Low-Temperature Plasma and Graphene: An in situ Raman Thermometry Study, Phys Rev Appl. 15 (2021). https://doi.org/10.1103/PhysRevApplied.15.024018.

[29] L. Fayette, B. Marcus, M. Mermoux, N. Rosman, L. Abello, G. Lucazeau, In situ Raman spectroscopy during diamond growth in a microwave plasma reactor, J Appl Phys. 76 (1994) 1604–1608. https://doi.org/10.1063/1.357740.

[30] S. Nakashima, H. Harima, Raman investigation of SiC polytypes, Physica Status Solidi A Appl Res. 162 (1997) 39–64. https://doi.org/10.1002/1521-396X(199707)162:1<39::AID-PSSA39>3.0.CO;2-L.

[31] D.W. Feldman, J.H. Parker, W.J. Choyke, L. Patrick, Raman Scattering in 6H Si, Physical Review. 170 (1968) 698–704. https://doi.org/10.1103/PhysRev.170.698.

[32] A. Turos, H. Frey, O. Meyer, W. Müller, J.M. Pirrung, Ion beam analysis of amorphous silicon films produced by magnetron sputtering, Physica Status Solidi (a). 83 (1984) 437–443. https://doi.org/10.1002/pssa.2210830203.

[33] M. MacIas-Montero, F.J. Garcia-Garcia, R. Álvarez, J. Gil-Rostra, J.C. González, J. Cotrino, A.R. Gonzalez-Elipe, A. Palmero, Influence of plasma-generated negative oxygen ion impingement on magnetron sputtered amorphous SiO 2 thin films during

growth at low temperatures, J Appl Phys. 111 (2012). https://doi.org/10.1063/1.3691950.

[34] L.N. He, J. Xu, Properties of amorphous SiO2 films prepared by reactive RF magnetron sputtering method, Vacuum. 68 (2002) 197–202. https://doi.org/10.1016/S0042-207X(02)00388-3.

[35] M. Mayer, SIMNRA, a simulation program for the analysis of NRA, RBS and ERDA, in: AIP Conf Proc, AIP, 1999: pp. 541–544. https://doi.org/10.1063/1.59188.

[36] Wei-Kan Chu, James W. Mayer, Marc A. Nicolet, Backscattering Spectrometry, 1st edition, 1978. https://www.elsevier.com/books/backscattering-spectrometry/chu/978-0-12-173850-1 (accessed February 28, 2023).

[37] M.M. Lucchese, F. Stavale, E.H.M. Ferreira, C. Vilani, M.V.O. Moutinho, R.B. Capaz, C.A. Achete, A. Jorio, Quantifying ion-induced defects and Raman relaxation length in graphene, Carbon N Y. 48 (2010) 1592–1597. https://doi.org/10.1016/j.carbon.2009.12.057.

[38] E.H. Martins Ferreira, M.V.O. Moutinho, F. Stavale, M.M. Lucchese, R.B. Capaz, C.A. Achete, A. Jorio, Evolution of the Raman spectra from single-, few-, and many-layer graphene with increasing disorder, Phys Rev B. 82 (2010) 125429. https://doi.org/10.1103/PhysRevB.82.125429.

[39] L. Gustavo Cançado, M. Gomes da Silva, E.H. Martins Ferreira, F. Hof, K. Kampioti, K. Huang, A. Pénicaud, C. Alberto Achete, R.B. Capaz, A. Jorio, Disentangling contributions of point and line defects in the Raman spectra of graphene-related materials, 2d Mater. 4 (2017) 025039. https://doi.org/10.1088/2053-1583/aa5e77.

[40] P. Vinchon, X. Glad, G. Robert Bigras, R. Martel, L. Stafford, Preferential self-healing at grain boundaries in plasma-treated graphene, Nat Mater. 20 (2021) 49–54. https://doi.org/10.1038/s41563-020-0738-0.

[41] G. Robert Bigras, X. Glad, P. Vinchon, R. Martel, L. Stafford, Selective nitrogen doping of graphene due to preferential healing of plasma-generated defects near grain boundaries, NPJ 2D Mater Appl. 4 (2020) 42. https://doi.org/10.1038/s41699-020-00176-y.

[42] M. Bruna, A.K. Ott, M. Ijäs, D. Yoon, U. Sassi, A.C. Ferrari, Doping Dependence of the Raman Spectrum of Defected Graphene, ACS Nano. 8 (2014) 7432–7441. https://doi.org/10.1021/nn502676g.

[43] F. Banhart, J. Kotakoski, A. v. Krasheninnikov, Structural Defects in Graphene, ACS Nano. 5 (2011) 26–41. https://doi.org/10.1021/nn102598m.